

A design for the generation of temporally-coherent radiation pulses in the VUV and beyond by a self-seeding high-gain free electron laser amplifier

B W J McNeil^{1,4}, N R Thompson^{1,2}, D J Dunning²,
J G Karssenberg³, P J M van der Slot³ and K-J Boller³

¹ Scottish Universities Physics Alliance, Department of Physics,
University of Strathclyde, Glasgow, G4 0NG, UK

² Accelerator Science and Technology Centre, Science and Technology
Facilities Council Daresbury Laboratory, Warrington, WA4 4AD, UK

³ Laser Physics and Nonlinear Optics Group, MESA+ Institute for
Nanotechnology, University of Twente, PO Box 217, 7500 AE Enschede,
The Netherlands

E-mail: b.w.j.mcneil@strath.ac.uk, n.r.thompson@dl.ac.uk and
p.j.m.vanderslot@tnw.utwente.nl

New Journal of Physics **9** (2007) 239

Received 23 April 2007

Published 20 July 2007

Online at <http://www.njp.org/>

doi:10.1088/1367-2630/9/7/239

Abstract. A proposal for a self-seeding, tunable free-electron laser amplifier operating in the vacuum ultra-violet (VUV) region of the spectrum is presented. Full three-dimensional (3D) modelling of the free electron laser and the optical feedback system has been carried out. Simulations demonstrate the generation of near transform limited radiation pulses with peak powers in the hundreds of megawatts. Preliminary 1D simulations show that by using a similar system it may be possible to extend such operation beyond the VUV to higher photon energies.

⁴ Author to whom any correspondence should be addressed.

Contents

1. Introduction	2
2. 1D simulations	4
3. VUV-FEL design parameters	6
4. 3D simulations	8
4.1. The simulation code	8
4.2. Steady-state simulations	9
4.3. Cavity effects	10
4.4. Time dependent simulations	17
5. RAFEL operation at higher photon energies	18
5.1. SASE results	19
5.2. Very low feedback RAFEL results	19
6. Conclusion	21
Acknowledgments	22
References	22

1. Introduction

The 4th generation light source (4GLS) facility is proposed by the UK's Science and Technology Facilities Council (STFC) Daresbury Laboratory [1] to meet the needs of a wide range of science research requiring high brightness synchronized sources from THz frequencies to photon energies of 100 eV. The facility will comprise a range of sources including synchrotron radiation sources, free-electron lasers (FELs) and conventional lasers, which will be combined synchronously to allow innovative pump-probe experiments [2]–[4].

The two most important differences between 4GLS and 3rd generation synchrotron facilities are the increased peak brightness, typically eight orders of magnitude due to the greatly improved temporal coherence, and the shorter pulse lengths down to $\lesssim 100$ fs. While 3rd generation sources are able to characterize the structure of systems at the molecular level, the short pulse, high brightness, variably synchronized pump-probe techniques that will be employed at 4GLS will also enable short timescale process dynamics to be studied. The FEL sources will also generate fully variably polarized output.

The three main high-brightness sources of 4GLS are: in the extreme ultra-violet a high gain seeded FEL [5, 6] (XUV-FEL) generating photon energies between 8–100 eV at peak power levels of 8–2 GW in pulses of ~ 50 fs full-width half-maximum (FWHM); an infra-red FEL (IR-FEL) operating between 2.5–200 μm with peak powers of between 1–20 MW in pulses of 0.3–30 ps FWHM [6]; and, the subject of this paper, a vacuum ultra violet FEL (VUV-FEL) operating within a small feedback low-Q cavity to generate photons in the energy range 3–10 eV.

The advanced sources of 4GLS will allow the study of a wide range of important new science and will rely heavily upon the synchronization of the sources in pump-probe type experiments. Specific studies requiring the VUV-FEL include [3, 4]: reflection anisotropy spectroscopy (RAS) of electrochemical interfaces e.g. the study of interactions between DNA sequences at metal-liquid interfaces; extension of sum frequency generated (SFG) spectral analysis over a wide spectral range when synchronized with the IR-FEL; circular dichroism microscopy, resonance Raman microscopy and time-resolved resonance Raman microscopy

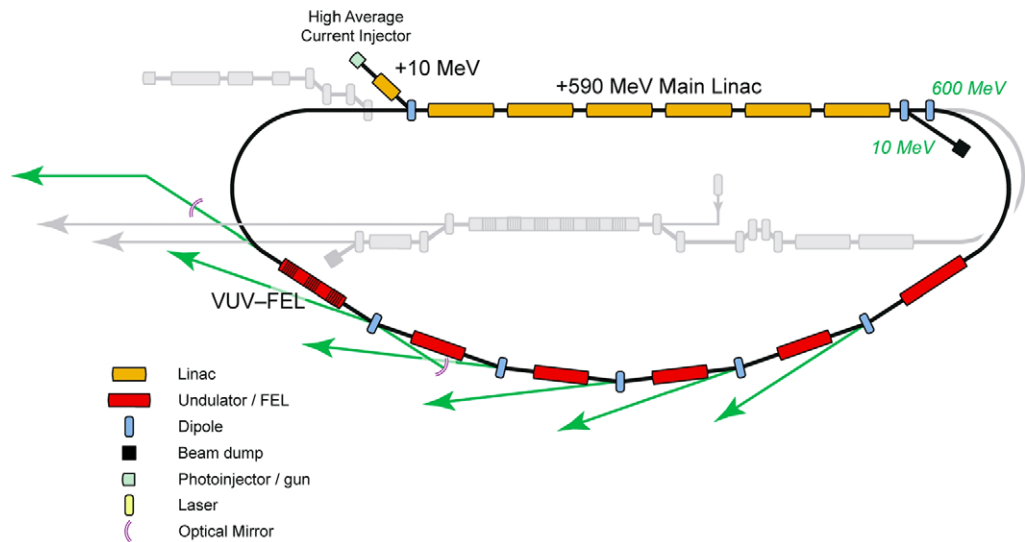


Figure 1. Schematic layout of the 4GLS conceptual design with the VUV-FEL branch highlighted in colour. Before electron bunches enter the VUV-FEL they pass through a distributed bunching system and may also generate radiation in five spontaneous radiation undulator sources.

allowing increased structural resolution and the study of the chemistry of sub-cellular domains in real time of proteins, carbohydrates and nucleic acids; the creation and study of transient, short-lived species such as those created in the upper atmosphere and interstellar dust clouds; the reaction pathways in asymmetric synthesis and of the origins of the homochirality of life; the measurement of ultra-fast charge and spin dynamics in optoelectronic nanomaterials, photovoltaics and magnetic semiconductors; and, when used with the XUV-FEL, the use of quantum chemical control to explore molecular evolution and chemical reactions.

A schematic of the 4GLS layout highlighting the VUV-FEL is shown in figure 1. The VUV-FEL will operate in the 600 MeV high average current branch of the energy recovery linac (ERL), being driven by ~ 80 pC electron bunches at up to 1.3 GHz. In addition to driving the VUV-FEL the electron bunches will be able to drive five upstream (US) spontaneous emission undulator sources. A system of distributed bunch compression between these US sources will achieve bunch lengths down to ~ 100 fs generating a peak current of ~ 300 A before injection into the VUV-FEL. Table 1 summarizes the VUV-FEL output as predicted by the analysis presented in this paper.

The design chosen for the VUV-FEL is based upon a high-gain amplifier system that utilizes a cavity with a low quality factor to generate a small amount of feedback [7]. This type of design was identified as being of particular interest for a short wavelength FEL such as the VUV-FEL where cavities are restricted by the available mirror reflectivities [7, 8]. Nevertheless, a small amount of feedback is sufficient to allow the FEL to achieve high-gain type saturation within a few cavity round trips. Such a system has also been termed a regenerative amplifier FEL (RAFEL) [8, 9]. A proposal has also been made to use narrow-bandwidth Bragg crystals as mirrors in a RAFEL configuration to generate a hard x-ray FEL [10]. This system relies upon the relatively narrow bandwidth of the Bragg reflections with respect to the FEL gain bandwidth to improve the temporal coherence of the output.

Table 1. Predicted VUV-FEL radiation output.

Tuning range	$\sim 3\text{--}10\text{ eV}$
Peak power	$\sim 500\text{--}300\text{ MW}$ (3 GW^a)
Repetition rate	$n \times 4\frac{1}{3}\text{ MHz}$ ($n \leq 300$, integer)
Polarization	Variable elliptical
Min pulse duration FWHM	170 fs (25 fs^a)
Typical $\Delta\nu\Delta t$	~ 1.0
Maximum pulse energy	$70\ \mu\text{J}$
Maximum average power	$n \times 300\text{ W}$

^aIndicates possible output in superradiant mode of operation.

It has been shown from preliminary one dimensional (1D) simulations of the VUV-FEL [11, 12] that the optimum outcoupling fraction is $\sim 75\%$ for mirrors of 60% reflectivity. This preliminary modelling predicts near maximum possible output power at a stable working point, so that the output power is relatively insensitive to small changes in outcoupling fraction or mirror reflectivity.

There are several expected advantages of the RAFEL over a low-gain oscillator FEL. As discussed, it can operate with low reflectivity mirrors in a region where high reflectivity is not available. The RAFEL should also be less sensitive to radiation-induced mirror degradation, and the small number of passes required to reach saturation should relax the longitudinal alignment tolerances. The optical feedback allows the undulator length to be reduced significantly compared to a self amplified spontaneous emission (SASE) FEL.

In this paper, the previous 1D modelling of the VUV-FEL is extended to full 3D simulations of the FEL interaction using Genesis 1.3 [13]. These Genesis 1.3 simulations have been integrated with a new 3D optics simulation code optical propagation code (OPC) [14] which models radiation transport outwith the FEL interaction region of the hole out-coupled cavity to generate a full 3D simulation of the VUV-FEL. These simulations confirm the validity of the 4GLS conceptual design report (CDR) design [6, 11, 12] and allow proper modelling of the cavity resonator over the 3–10 eV operational range. An analysis of the temporal coherence of the output at 10 eV demonstrates significant improvements over SASE generating near Fourier transform limited pulse output.

Preliminary results of 1D modelling are also presented for a system with a low feedback factor that returns only 10^{-5} of the undulator output. Such low feedback may occur when mirror reflectivities are very poor, for example with a RAFEL system attempting operation into the XUV and x-ray regions of the spectrum. The results are good and suggest that in principle a low feedback RAFEL may prove a viable source at much higher photon energies.

2. 1D simulations

In this section the previous 1D simulation results of [6, 11, 12] which describe the initial 4GLS VUV-FEL design are summarized to demonstrate the RAFEL concept and allow comparison with the following 3D simulations.

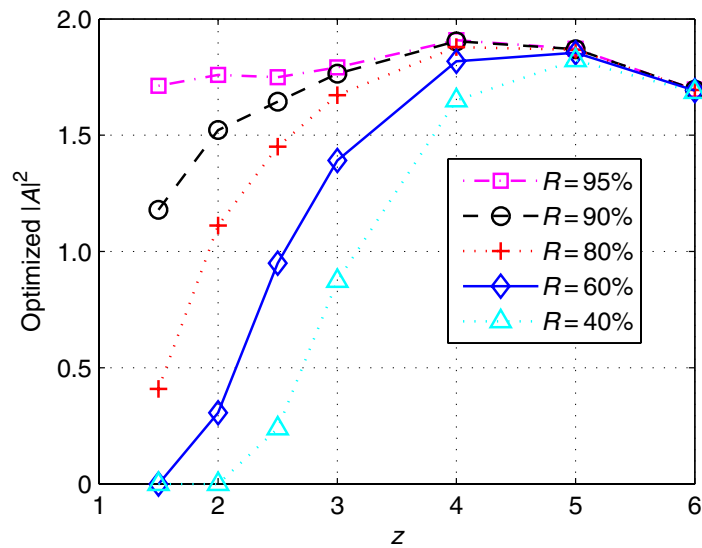


Figure 2. The maximum scaled output power $|A|^2$ at saturation as a function of scaled undulator length \bar{z} for a range of mirror reflectivities.

Some optimization of cavity mirror reflectivity and outcoupling fraction is first performed in the steady-state regime, where temporal pulse effects are neglected. In figure 2 the maximum scaled output power $|A|^2$ at saturation, maximized with respect to the outcoupling fraction, is plotted as a function of universally scaled FEL interaction length $\bar{z} = z/l_g$ for several mirror reflectivities. Here $l_g = \lambda_u/4\pi\rho$ is the nominal 1D gain length, λ_u is the undulator period and ρ is the FEL parameter [15]. It is seen that for $\bar{z} = 4$ this maximized power is relatively insensitive to the mirror reflectivity—mirror reflectivities of 60% yield a power only 5% lower than that obtained using 95% reflectivity mirrors. While these results for the outcoupling fraction that maximizes the output power are encouraging it is important to examine the sensitivity of the output as a function of the outcoupling fraction to ensure stability with respect to changes in the outcoupling. This is shown in figure 3 for $\bar{z} = 4$ and for three mirror reflectivities $R = 40, 60$ and 95%. For mirror reflectivity $R = 60\%$, the outcoupling fraction that maximizes the output power is seen to be 92% and it is also seen that a small increase above 92% would prevent lasing to saturation. Thus, any minor electron beam instabilities or fluctuations in the transverse optical mode could stop lasing. It is therefore preferable to operate with a lower outcoupling, of say 75%, at the expense in a small decrease in output power to achieve a greater stability. Indeed, with a fixed outcoupling of 75% the output power is seen to *increase* with a *decrease* in the mirror reflectivity. This may be explained from the slight over-saturation of the single pass high-gain FEL mechanism, due to the lower power outcoupling, and has the practical advantage that any mirror degradation will reduce the power feedback which acts as the seed field. This reduced seed decreases the over-saturation and results in an increase in the power output.

When temporal pulse effects are included then the length of the cavity with respect to the rate at which the electron bunches enter the FEL becomes important [16]–[20]. This is demonstrated in the results of 1D simulations presented in [12] and shown in figure 4 where the saturated peak power and FWHM pulse width are plotted as a function of cavity detuning. (A positive detuning corresponds to a shortening of the cavity.) The dependence of the peak power and pulse width upon cavity detuning is very similar to that of low-gain oscillator

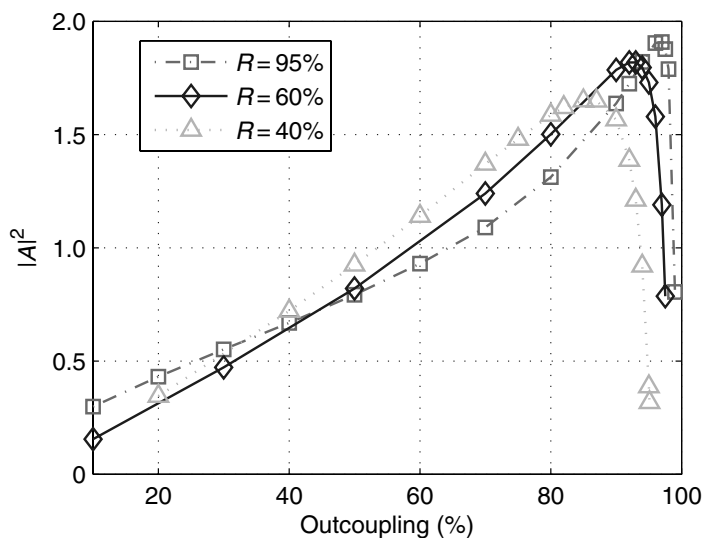


Figure 3. Scaled output power $|A|^2$ as a function of outcoupling fraction, for mirror reflectivities $R = 40, 60$ and 95% and for a scaled undulator length $\bar{z} = 4$.

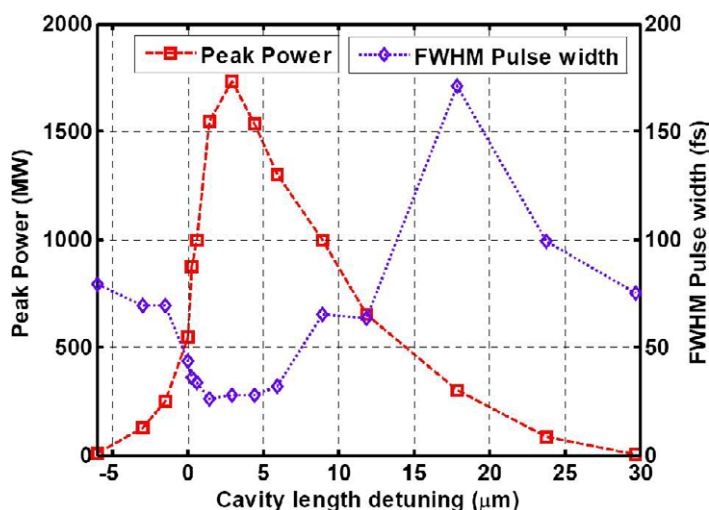


Figure 4. Radiation pulse peak power (red) and FWHM pulse width (blue) as a function of cavity detuning for 1D VUV-FEL simulations operating at photon energy of 10 eV.

FELs [16, 17, 20]. As with these systems, there is a significant increase in peak power and pulse shortening close to cavity resonance which in the low-gain system is due to superradiant behaviour [18, 19]. We speculate, but have not proven, that the same superradiant effects are present in the 1D simulations of this high-gain system.

3. VUV-FEL design parameters

The VUV-FEL is designed to generate radiation of variable polarization and will use APPLE-II variably polarized undulator modules. The following parameters have been selected using

Table 2. VUV-FEL parameters for 10 eV operation.

Undulator	
Undulator period λ_w	60 mm
Periods per module	37
Number of modules	5
Electron beam	
Electron beam energy	600 MeV
Relative energy spread (rms)	0.1%
Bunch charge	80 pC
Peak current	300 A
Normalized emittance	2 mm-mrad
Optical cavity	
Cavity length L_{cav}	34.6 m
US ROC r_1	12.85 m
Downstream (DS) ROC r_2	22.75 m
Rayleigh length z_R	2.8 m
Fundamental mode waist w_0	0.34 mm
Waist position (measured from US mirror)	12.2 m
Outcoupling hole radius	2 mm
Cavity stability $g_1 \times g_2$	0.88

simple analysis and the FEL design formulae of Xie [21]. A summary of the design parameters are given in table 2 and a schematic shown in figure 5 where the fundamental cold-cavity mode is shown on the same longitudinal scale as the machine layout.

An undulator period of 60 mm enables the photon energy range 3–10 eV to be covered by undulator gap tuning from 10–19 mm in helical mode and 12–25 mm in planar mode. For sufficient gain for RAFEL operation the undulator length must give a gain equivalent in the 1D limit to $\bar{z} \geq 4$ over all wavelengths and polarisations. The required length is found using the Xie formulae [21] to be 11 m and is achieved with five 2.2 m modules of 37 periods. An inter-module gap of 0.6 m allows space for a focusing quadrupole, beam position monitor and phase matching unit. A FODO focusing lattice is used with each quadrupole of length 0.12 m and of strength 9 T m^{-1} .

The resonator parameters were initially derived from simple cold-cavity assumptions. The fundamental cold-cavity mode is focused to maximize the transverse overlap, and hence FEL coupling, between radiation and electron beam over the first two undulator modules. This is achieved with a waist at the end of the first module, ~ 12.2 m from the US mirror as shown in figure 5. The optimum Rayleigh length z_R for maximum overlap is then approximately one third the total length of the two modules plus gap, i.e. $z_R \sim 1.7$ m. However, for this Rayleigh length the cavity geometry is close to instability and gives an excessive waist radius at the downstream (DS) mirror and some diffraction losses on the undulator aperture for the longer wavelengths. Furthermore, the outcoupling hole radius on the DS mirror is larger than the waist radius of the spontaneous radiation emitted on the first pass and does not allow sufficient feedback. A Rayleigh length was therefore chosen so that the waist radius of the fundamental cavity mode

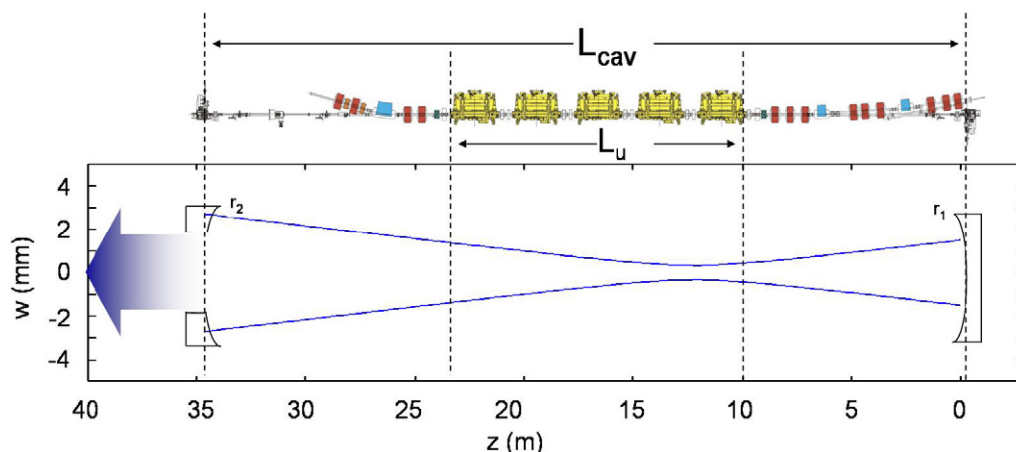


Figure 5. A schematic of the 4GLS VUV-FEL with the baseline design parameters. The fundamental cavity mode at $1/e^2$ of the on-axis intensity is shown in blue on the same longitudinal scale as the engineering representation. Electron beam transport is right to left.

is the same as the estimated waist radius of the spontaneous emission. This gives a Rayleigh length of 2.8 m, somewhat larger than the value for maximum overlap.

The outcoupling hole radius is chosen so that the outcoupling fraction of the fundamental cold-cavity mode is 65%. While this is less than the 75% value suggested by the 1D simulations, the high-gain FEL interaction will guide the radiation so reducing the waist radius and increase the outcoupling fraction towards its optimum value. A mirror material of protected aluminium with a reflectivity of 60% at 10 eV is assumed [22].

4. 3D simulations

Previous modelling of the VUV-FEL has been carried out using a 1D model and also one that used the 3D code Genesis 1.3 for the FEL interaction, but a greatly simplified cavity model that approximated the cavity feedback as a simple attenuator of the FEL output [11, 12]. The latter model has been greatly improved by incorporating a proper modelling of the cavity. A new simulation code, OPC, has been developed which simulates in 3D the optical components and radiation propagation within the non-amplifying sections of the optical cavity [14]. OPC works together with Genesis 1.3 to simulate a complete FEL cavity configuration. A summary of the combined OPC-Genesis 1.3 simulation code is presented before using it to model the VUV-FEL operating at 10 and 3 eV in steady-state mode. Analyses of the transverse radiation characteristics are presented and scans over cavity geometry parameters are performed in a first-attempt performance optimization. The OPC-Genesis 1.3 simulation code is then used in time-dependent mode to examine the temporal coherence of the radiation output.

4.1. The simulation code

The OPC [14, 23] models propagation of a monochromatic radiation field in the paraxial approximation between an input and an output plane. OPC is able to implement three different

methods for propagation: the spectral method (SM), the Fresnel diffraction integral (FDI) and a modified FDI (MFDI). The MFDI includes the total ABCD matrix of the optical system that is present between the input and output plane. All three propagation methods are numerically implemented using fast Fourier transforms (FFTs), however the SM allows a more efficient numerical implementation and is computationally the fastest of the three [14, 23]. The drawback is that SM usually requires the largest transverse grid to avoid ‘numerical reflections’ of the wave at the grid boundary in the propagation region [24]. These reflections are not present when FDI or MFDI are used. Furthermore, MFDI has the advantage that it allows for a magnification factor between input and output plane despite the use of FFTs, and although the number of grid points is the same, their spacing need not be constant in the input and output plane [14]. Hence, using MFDI the grid can expand and follow the free space diffraction of an optical wave.

The resonator cavity FEL may be described as a gain section, i.e. the FEL amplifier, and the remainder of the optical cavity. Propagation of the radiation through the undulator is modelled by Genesis 1.3, while OPC propagates the optical field through the non-amplifying section of the resonator. Running both codes sequentially provides a single pass through the resonator. The two separate codes couple with each other through the electric field distribution of the optical wave that can be written to or read from file by each code. The Perl scripting language is used to both control the program flow and to define the resonator geometry. OPC has a functionality build into it that allows for parameter scans over both OPC and Genesis 1.3 input parameters.

Various optical components, such as lenses, mirrors, diaphragms, and hole coupled mirrors are available to construct optical resonators. The optical propagation code enables prediction of the output at each of the various optical elements, which is of advantage for beam diagnostics and for designing suitable optics for a further propagation of the output beam. It can also be used to determine the far field distribution of the out-coupled laser beam. The full functionality of Genesis 1.3 is maintained and resonator-based FELs can be modelled both in steady-state and time-dependent modes. Cavity detuning is realized through a control parameter already present in the Genesis 1.3 configuration file that controls the synchronization of the radiation pulse with the electron pulse at the entrance to the undulator.

4.2. Steady-state simulations

The parameters detailed in table 2 have been used for the initial simulations for 10 eV linearly polarized operation in the steady-state regime (i.e. neglecting temporal pulse effects). The growth of output power and the measured outcoupling fraction are shown in figure 6 as a function of the radiation cavity round trip pass number. At saturation the output power is 350 MW with an outcoupling fraction of $\sim 68\%$. Note that as the radiation power grows during the first few cavity round trips, the outcoupling is higher at $\sim 72\%$ and peaks at about 80% after ten round trips where the laser saturates. With further round trips the outcoupling drops and stabilizes at 68%. This simulation demonstrates the dynamic behaviour of the transverse optical mode of the laser beam as it builds up from noise to saturation.

In figure 7 the transverse power profiles, scaled with respect to the peak power, are plotted at saturation (round trip number twenty) at different points within the optical cavity: the undulator exit; incident on the hole out-coupled DS mirror; output from the outcoupling hole; reflected by the DS mirror; incident on the US mirror; and at the undulator entrance. It is clear that there is significant higher order transverse mode content in the radiation field. It is interesting that although the on-axis power of the radiation reflected from the DS outcoupling

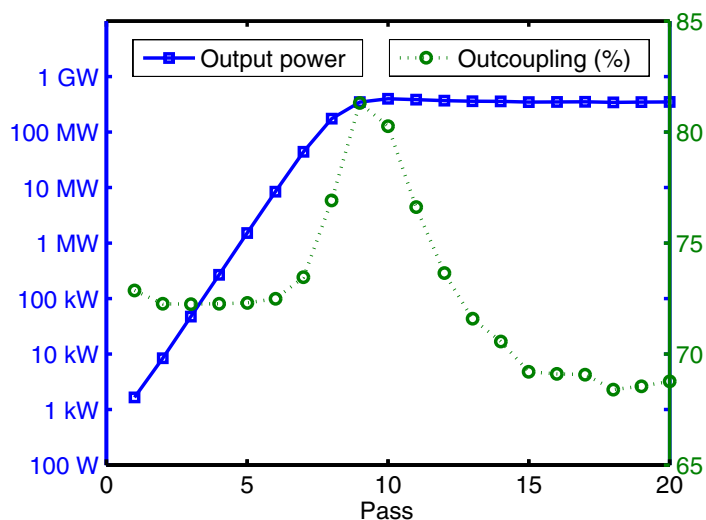


Figure 6. The radiation output power (blue) and the outcoupling percentage (green) as a function of cavity pass number for 10 eV operation.

mirror is zero, due to the outcoupling hole, by the time the radiation is transported through the cavity and reflected back into the undulator, the transverse power profile is transformed so that the peak power is on-axis. This allows the radiation to maintain good coupling with the electron beam and act as a seed for the next pass.

4.3. Cavity effects

A study has been done to investigate the effects of the hole outcoupled cavity upon the power and transverse mode structure of the output. The cavity parameters of mirror reflectivity, mirror geometry (affecting cold-cavity beam waist position and radius), and outcoupling hole radius have been varied about the initial design parameters of table 2. This is initially performed for 10 eV photon output, with results discussed in section 4.3.1, and then for 3 eV output, at the other end of the VUV-FEL operational range, in section 4.3.2. A wavelength dependent mirror reflectivity is introduced in section 4.3.3 to extend the results to the full photon energy range 3–10 eV.

4.3.1. 10 eV operation. In figure 8 the effect of varying the radius of the outcoupling hole and the mirror reflectivity on the saturated output power is plotted as a colour contour plot. (Saturation is defined to occur here after twenty cavity passes by which time actual saturation of the FEL output has occurred except perhaps at some of the extremes of the parameter ranges used in this and in the following simulation results.) The results show that the parameters as defined in the CDR [6] and reproduced in table 2 (output coupling hole radius 2 mm and mirror reflectivity 60%) give a satisfactory and stable output. In fact, in terms of the output power, these parameters are reasonably close to the optimum as the power is near to its maximum and small changes in outcoupling hole radius and mirror reflectivity have only a small effect on the output power. The prediction of the simple 1D simulations, that a reduction in mirror reflectivity would cause a small increase in output power, is also demonstrated to be valid in 3D

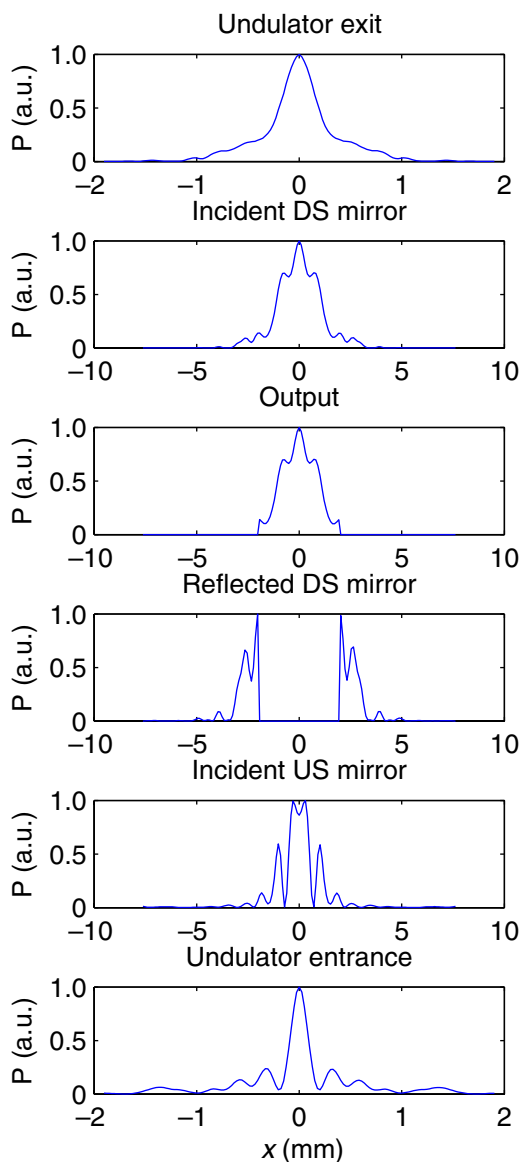


Figure 7. Power cross-sections at saturation, scaled with respect to their peak values, for different positions within the optical cavity. The parameters are those of the CDR (table 2) with cold-cavity waist position 12.2 m and waist radius 0.34 mm.

simulations. Therefore, in what follows, unless explicitly stated otherwise, a mirror reflectivity of 60% is assumed for operation at 10 eV.

Different cavity configurations have been investigated by changing the radius of curvature (RoC) of the mirrors so that either the waist radius of the lowest order cold-cavity mode, or the waist position within the cavity, is kept constant while the other was varied. The dependence of the output power on hole radius and waist position is shown in figure 9. It is seen that the waist position which gives a relatively broad region of stable power output is at ~ 10.5 m from the US mirror. This differs slightly from the CDR value of 12.2 m from the US mirror.

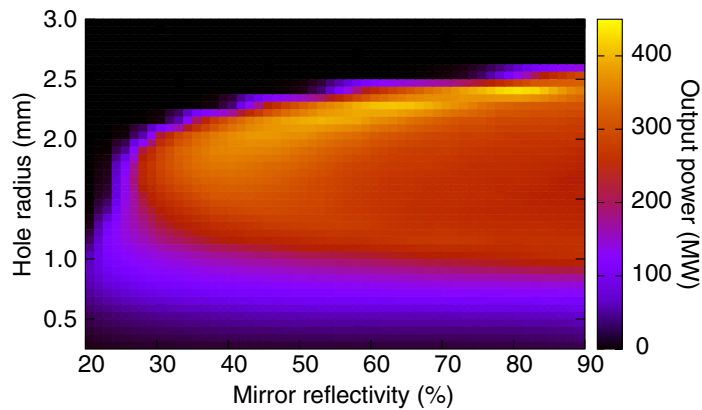


Figure 8. Output power as a function of outcoupling hole radius and mirror reflectivity. The CDR parameters are an outcoupling hole radius of 2 mm and mirror reflectivity of 60%.

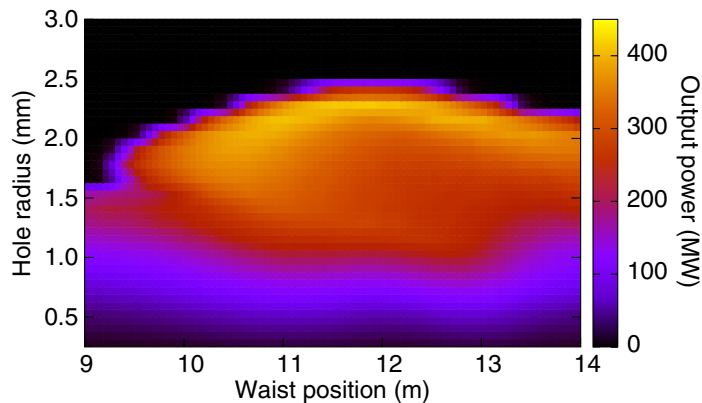


Figure 9. Output power as a function of outcoupling hole radius and cold-cavity waist position, for a waist radius of 0.34 mm.

From figure 10 it can be seen that for a cold-cavity waist position of 12.2 m from the US mirror there is little dependence on the cold-cavity waist radius even when the waist radius is 0.1 mm which corresponds to the transition to an unstable resonator cavity case where the cavity stability parameter $g_1g_2 = 1$. This region of the unstable resonator case has not yet been investigated but may prove an interesting topic for future research. Similar results were obtained for a waist position of 10.5 m from the US mirror. This leads to the conclusion that consideration of cold-cavity resonator modes are not very relevant to this design as the effects of gain-guiding of the radiation by the high-gain FEL interaction effectively forces the beam waist toward the end of the undulator and strongly dominates cavity mode effects. This conclusion is supported by the following simulations investigating the effect of changes in cold-cavity waist position on the radiation transverse power profiles at different cavity positions.

The transverse cross-section of the intensity as a function of waist position at the input to the undulator is shown in figure 11. This is consistent with the previous results of figure 7 and demonstrates that the power is peaked on axis to act as an effective seed which couples to the electron bunches entering the undulator.

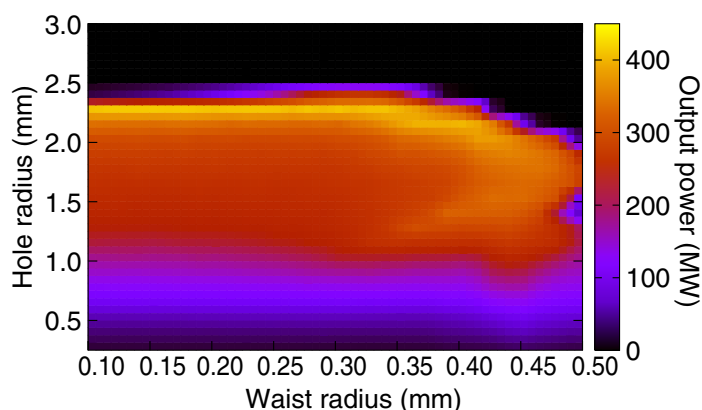


Figure 10. Output power as a function of outcoupling hole radius and cold-cavity waist radius, for waist position of 12.2 m.

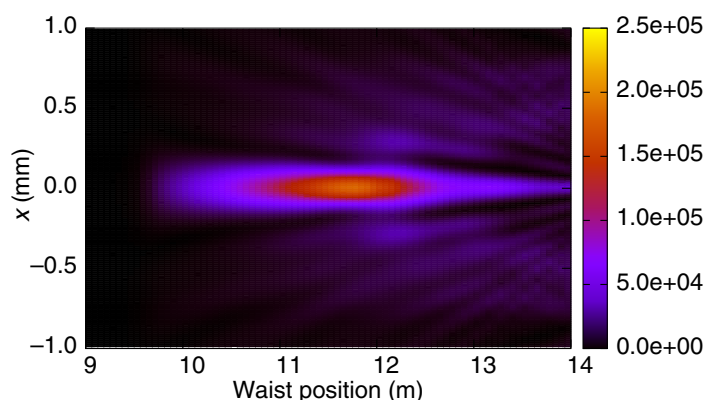


Figure 11. Intensity (a.u.) cross-section at the undulator entrance as a function of the cold-cavity waist position of the fundamental mode of the resonator for a outcoupling hole radius of 2 mm.

Plotted in figure 12 is the far-field intensity transverse cross-section calculated at 14 m beyond the 2 mm radius outcoupling hole, where the VUV-FEL design has optical diagnostics situated. Again the dependence on cold-cavity waist position is relatively weak. However, this far-field cross-section does display a significant higher order transverse mode structure, with a local minimum intensity on axis. The effect of output-coupling hole radius on the far-field cross-section is shown in figure 13. While the far field cross-section can be improved to more closely approximate a fundamental Gaussian mode by reducing the hole radius to ~ 1 mm, this has the consequence of reducing the output power by a factor $\gtrsim 2$ as may be seen from figures 8 to 10. Nevertheless, the form of the transverse profile will be an important consideration and dependent upon the experimental requirements and will need to be considered further in consultation with potential users.

Finally the total power, as a function of distance through the undulator and of the cold-cavity waist position, is plotted in figure 14. The waist position of the initial design parameters of 12.2 m is seen to give the largest power growth rate, with values about this waist position giving saturation nearer the end of the undulator.

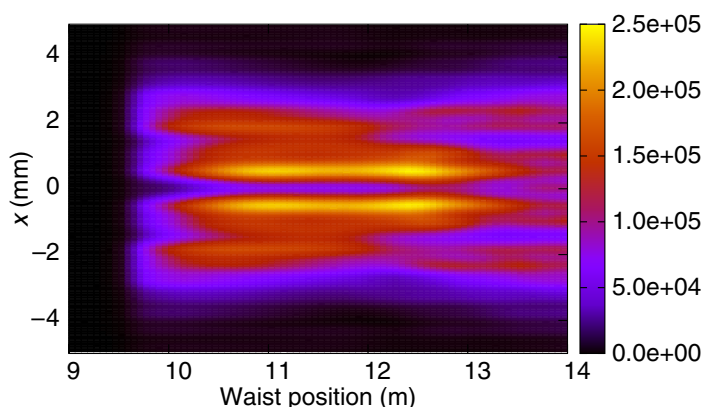


Figure 12. Intensity (a.u.) cross-section in the far field as a function of the cold-cavity waist position of the fundamental mode of the cavity for an outcoupling hole radius of 2 mm.

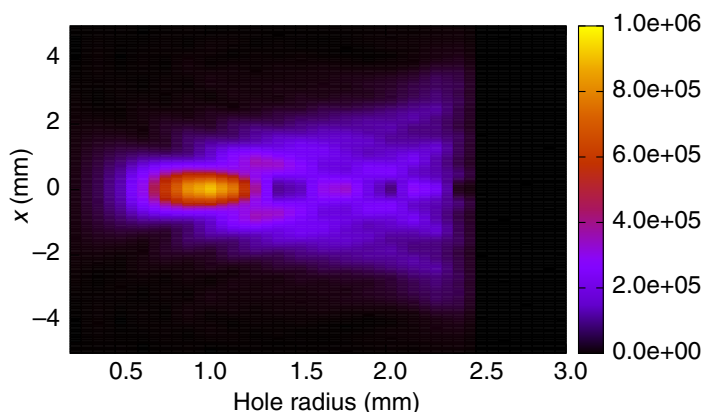


Figure 13. Intensity (a.u.) cross-section in the far field as a function of outcoupling hole radius, for cold-cavity waist position 12.2 m.

Further detailed optimization will be carried out to maximize the output power while maintaining an optimum far-field cross-section. This will include an investigation of unstable resonators with cavity stability parameters $g_1 g_2 > 1$. The effects of optical transport on this transverse modal structure have yet to be investigated.

4.3.2. 3 eV optimization. Simulations similar to the previous section have been performed for a photon energy of 3 eV. This corresponds to the opposite end of the spectral range of operation of the VUV-FEL. In figure 15 the output power is plotted as a function of out-coupling hole radius and cold-cavity waist position, corresponding to figure 9 for 10 eV operation. The initial design value for the waist position was 12.2 m. The plot of figure 15 shows that the output power may be increased by changing the waist position to 10 m. From figure 5 it is seen that this waist position is at the entrance of the undulator. For 10 eV operation the optimum waist position was ~ 10.5 m and this appears a reasonable compromise for the 3 eV case. With this waist position, the output power is plotted in figure 16 as a function of waist radius and hole radius. As for the 10 eV case of figure 10, the waist radius of the fundamental cold-cavity mode has minimal

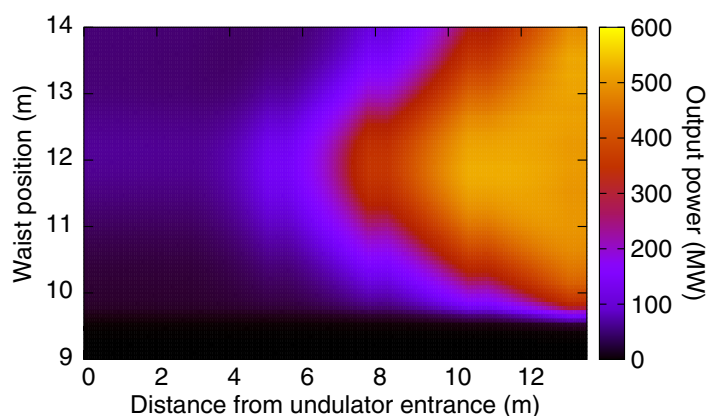


Figure 14. Radiation power along the undulator as a function of the cold-cavity waist position. The slight regular vertical band structure in the plot is due to the gaps between undulator sections.

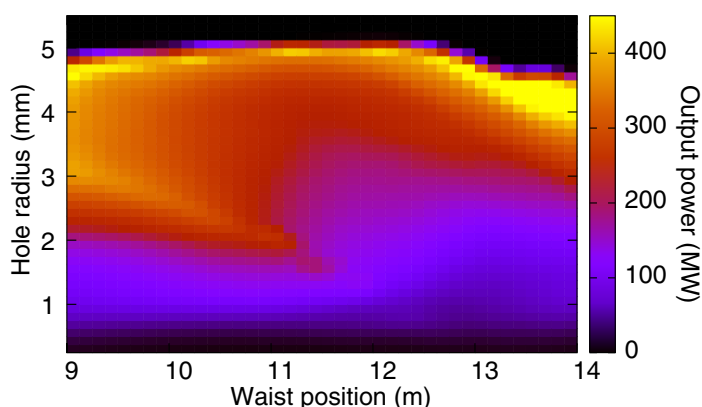


Figure 15. The output power as a function of outcoupling hole radius and cold-cavity waist position for 3 eV photon output.

effect on the output power below approximately 0.4 mm. For larger values of the waist radius the behaviour appears quite complex and requires further analysis. Note that in figure 16 a greater range of the waist radius up to 0.7 mm has been considered when compared with the 10 eV case of figure 10 which is plotted for waist radius up to only 0.5 mm.

4.3.3. 3–10 eV operation. A disadvantage of mirror hole out-coupling is that the out-coupling fraction is wavelength-dependent because the mode radius at the mirror is proportional to the square root of the wavelength. In order to assess the tuning ranges available from a mirror with fixed hole radius the output power is plotted as a function of hole radius over the photon energy range 3–10 eV. The mirror reflectivity has been assumed to vary linearly with photon energy from 85% at 3 eV to 60% at 10 eV. From the 3 and 10 eV results above a cold-cavity waist position of 10.5 m gave good results for both photon energies. This waist position is therefore chosen for the other photon energies and the results are plotted in figure 17. Based on these results, three sets of mirrors with different out-coupling hole radii are proposed to cover the 3–10 eV range and are summarized in table 3.

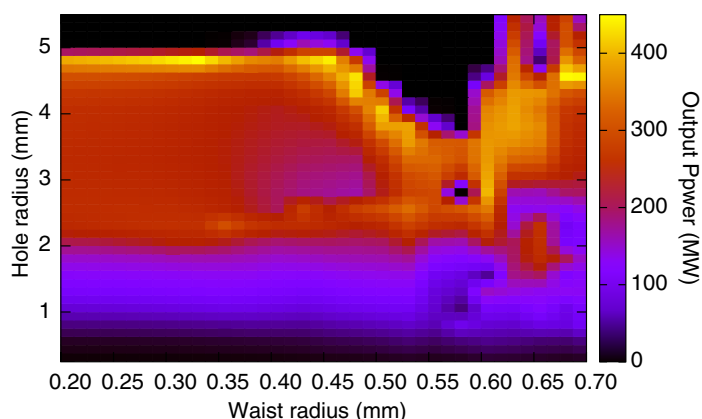


Figure 16. Output power as a function of outcoupling hole radius and cold-cavity waist radius for 3 eV photon operation with the waist position of 10.50 m from the US mirror.

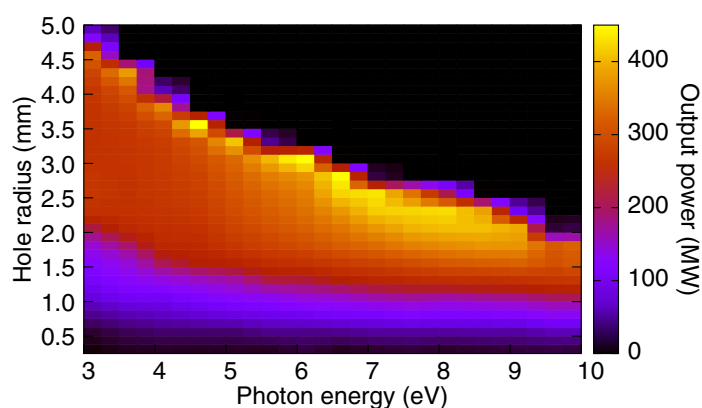


Figure 17. The output power as a function of photon energy and mirror outcoupling hole radius. The mirror reflectivity varies linearly with photon energy from 85% at 3 eV to 60% at 10 eV.

Table 3. Summary of mirror sets.

	R_1 (m)	R_2 (m)	Hole radius (mm)	Tuning range (eV)	Output power (MW)
A	10.57	24.11	2.5	3.0–6.5	250–400
B	10.57	24.11	2.0	3.5–9.0	250–400
C	10.57	24.11	1.5	6.5–10.0	250–300

Table 3 shows that the full photon energy range may be covered with only two mirror sets (A and C). However, using a third mirror set (B) gives the user the largest tuning range from 3.5 to 9 eV with a single mirror set. Indeed, it would also be possible to use this single mirror to cover the complete 3–10 eV tuning range, however, as seen from figure 17, the output powers attainable would be slightly reduced from the 250–400 MW. Table 3 also demonstrates that a

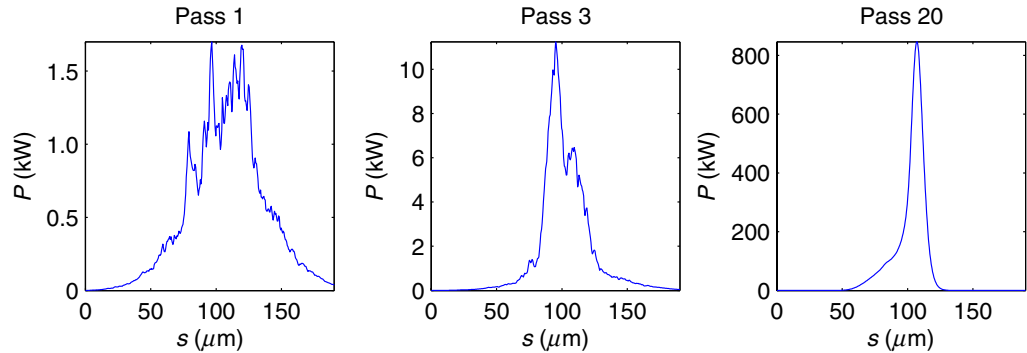


Figure 18. 3D simulation of the radiation output pulse power for VUV-FEL operation at 10 eV after 1, 3 and 20 passes.

single cavity resonator geometry may be used with only the outcoupling hole needing to be altered. This should allow for a relatively simple design and alignment of the cavity.

4.4. Time dependent simulations

3D time-dependent simulations have been performed to investigate the VUV-FEL radiation pulse properties. In addition to the peak pulse powers, of great importance to potential users of the radiation is the longitudinal coherence as measured by the time–bandwidth product.

The VUV-FEL design parameters of table 2 are used for a photon energy operation of 10 eV with the cavity detuning close to synchronism. Cavity detuning is synchronous when the cavity round-trip time for the radiation, $2L_{\text{cav}}/c$, is equal to an integer multiple of the period between successive electron bunches. Previous studies of FEL resonator cavities have shown that close to synchronism the FEL interaction moves toward a superradiant evolution where the radiation power scales as the peak electron bunch current squared [6, 19]. This superradiant behaviour generates higher peak powers than predicted by steady-state theory and generates narrow pulses. Similar pulse behaviour was reported from the 1D simulations of the VUV-FEL simulations of [12] and reproduced in figure 4. While superradiance has not been explicitly tested for, the pulse narrowing and larger peak powers associated with superradiance are observed in the 3D simulations.

The pulse power profiles of figure 18 for the VUV-FEL design operation at 10 eV are seen to be relatively smooth only after three cavity passes when compared to the relatively noisy output after the first pass through the cavity. Here, the parameter s is the distance as measured from the ‘tail’ of the electron bunch. These results are in good agreement with those of the 1D simulations summarized in figure 4. This improved power profile is indicative of the development of temporal coherence in the output pulses. Furthermore, after twenty passes saturation occurs and the pulse length has reduced significantly suggesting a superradiant-type pulse evolution.

A more complete analysis has been carried out to quantify the development of the temporal coherence by recording at the end of each cavity pass the pulse time–bandwidth product as defined by:

$$\Delta\nu\Delta t = \frac{1}{\lambda} \left(\frac{\Delta\lambda}{\lambda} \right) \Delta z,$$

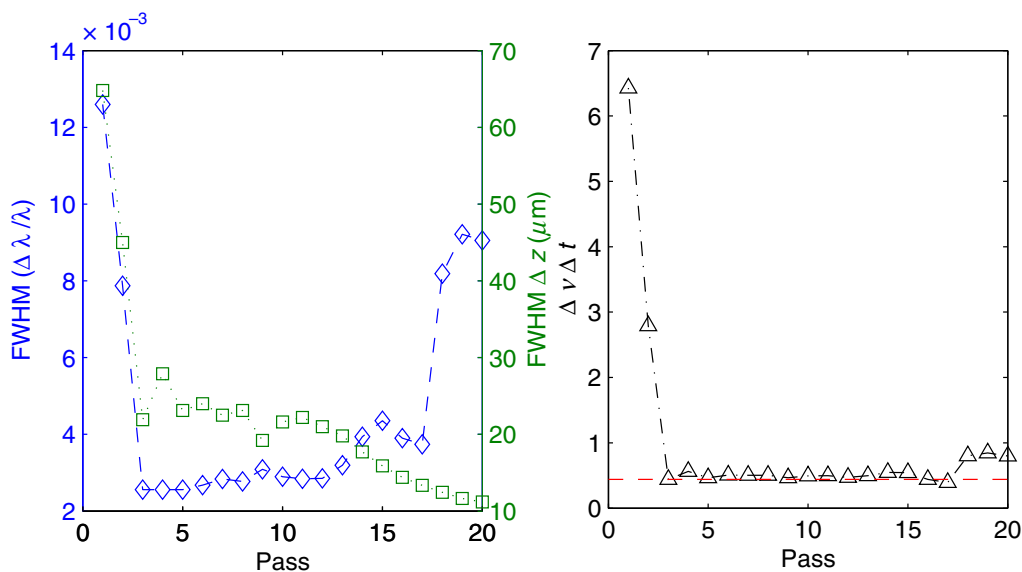


Figure 19. The left hand figure plots the radiation pulse FWHM linewidth and FWHM pulse length. The right hand figure shows the calculated time–bandwidth product $\Delta\nu\Delta t$. The dotted red line shows, for reference, the time–bandwidth product of a transform limited Gaussian pulse ($\Delta\nu\Delta t = 0.44$).

where Δz is the pulse width. The numerical value obtained depends upon the definition of width. For the analysis here FWHM values are used and for this case a Fourier transform-limited Gaussian pulse has a time–bandwidth product $\Delta\nu\Delta t \simeq 0.44$. In figure 19 the development of the FWHM linewidth, FWHM pulse length and the time–bandwidth product are plotted for the first 20 passes. It is seen that only after three passes the time–bandwidth product is approximately equal to that of a transform limited Gaussian. The increase in the bandwidth from pass 17 is seen to increase the time–bandwidth product. It has been observed from 1D simulations that this type of behaviour is dependent upon the cavity detuning and can be greatly reduced for some cavity detunings. It is thought that the behaviour is related to the work of [18] and this is the subject of ongoing research.

Simulations carried out with a 1D time-dependent code are in good agreement with this result for cavity lengths close to synchronism [6, 12]. These 1D simulations also show that in the quasi steady-state regime, where the cavity is detuned to offset the effect of pulse lethargy (cavity length detuning of $\sim 15\mu\text{m}$ in figure 4), the coherence develops equally rapidly with time–bandwidth products at saturation of $\Delta\nu\Delta t \simeq 1.0$.

5. RAFEL operation at higher photon energies

The above results present a specific design for the 3–10 eV photon energy VUV-FEL of the 4GLS project in which the minimum required cavity feedback is of the order of a few percent, although potentially more stable output could be obtained for $\sim 10\%$. The feedback provides a seed pulse which is of sufficient intensity to dominate the shot noise power in the electron beam, enabling the subsequent high-gain FEL mechanism to develop output of good temporal coherence generating close to transform-limited pulses.

The possibility of operating a RAFEL at higher photon energies, into the XUV and possibly beyond, is now considered. There is a general trend of reduced mirror reflectivity towards higher photon energies and this will diminish the feedback obtainable. A possible exception is via the use of Bragg-type crystal mirrors, employed in the design proposed in [10]. However, the need to satisfy the Bragg condition restricts the ability to tune the FEL.

A minimum feedback fraction will be required to ensure that the temporal coherence is retained pass-to-pass because the power returned by the cavity to the start of the undulator must be sufficient to dominate the electron beam shot noise. As the feedback fraction is decreased so the FEL interaction length must be increased to achieve saturation. In the limit where the power feedback is less than that due to shot-noise the FEL reverts to a SASE FEL. It can be shown from [25] that in the universal scaling of [15] the shot-noise power is:

$$|A_0|^2 \approx \frac{6\sqrt{\pi}\rho}{N_\lambda \sqrt{\ln(N_\lambda/\rho)}},$$

where N_λ is the number of electrons per radiation wavelength. At saturation the scaled saturated power is $|A_{\text{sat}}|^2 \sim 1$ and so the scaled power acting as seed at saturation is $F|A_{\text{sat}}|^2 \sim F$, where F is the fractional feedback factor of the cavity. Hence the requirement that the power feedback will dominate the shot-noise power may be written:

$$F \gg \frac{6\sqrt{\pi}\rho}{N_\lambda \sqrt{\ln(N_\lambda/\rho)}}.$$

The 1D time-dependent simulation code FEL0 [12], which was used to generate the results of section 2, is now used to model a RAFEL with a very low feedback factor of $F = 10^{-5}$. An FEL parameter of $\rho = 2.9 \times 10^{-3}$ was used with a peak number of electrons per wavelength of $N_\lambda \approx 6.2 \times 10^5$. The condition on the feedback factor given above is then $F \gg 1.13 \times 10^{-8}$ which is seen to be satisfied. While these parameters are typical for an amplifier FEL operating with peak current of 2.4 kA at photon energy of 100 eV, they may be considered more general due to the universal scaling.

The scaled interaction length of the undulator amplifier was $\bar{z} = 8.67$ and the system simulated for 100 cavity passes with a small cavity detuning of $\delta_c = 2.0$ defined in units of the retarded time parameter $\bar{z}_1 = 4\pi\rho(z/\beta_\parallel - ct)/\lambda$ where the resonant electron axial velocity is $v_\parallel = c\beta_\parallel$ [12]. The scaled interaction length necessary for SASE saturation, i.e. without feedback, using these parameters is $\bar{z} \simeq 14$. This SASE case was simulated 200 times to enable comparison between the averaged SASE results and those of the RAFEL.

5.1. SASE results

The root mean square (rms) linewidth over 200 simulations for the SASE case was $\langle\sigma_\lambda/\lambda\rangle = 2.77 \times 10^{-3}$ with an rms pulse length $\langle\sigma_{\bar{z}_1}\rangle = 14.01$ giving a rms time-bandwidth product of $\langle\Delta\nu\Delta t\rangle = 5.9$. The rms peak intensity $\langle|A|_{\text{peak}}^2\rangle = 2.2$. A typical saturation pulse is shown in figure 20, this pulse being chosen as the time-bandwidth product, $\Delta\nu\Delta t = 6.0$, is approximately that of the mean for the SASE simulations.

5.2. Very low feedback RAFEL results

The results for the very low feedback RAFEL show a significant improvement in the quality of the pulse output with respect to SASE. The rms linewidth is reduced to $\langle\sigma_\lambda/\lambda\rangle \approx 1.1 \times 10^{-3}$

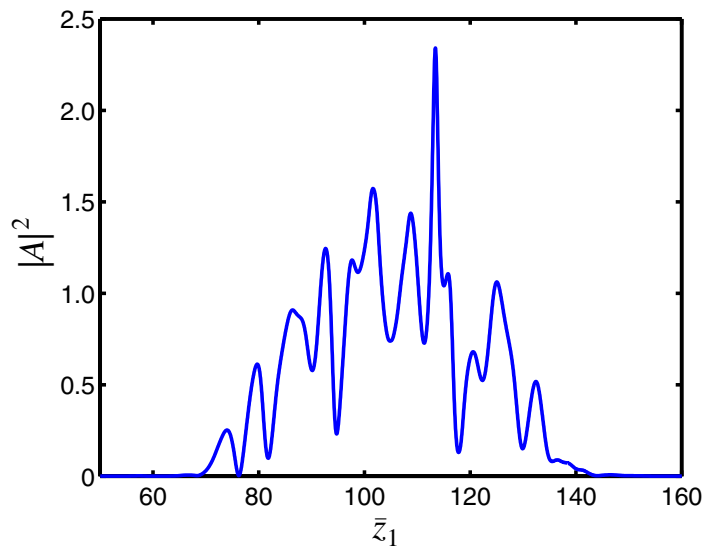


Figure 20. A representative SASE pulse at saturation. This case was chosen from the 200 simulations as its time–bandwidth product, $\Delta\nu\Delta t = 6.0$, which is approximately that of the mean of the 200 simulations.

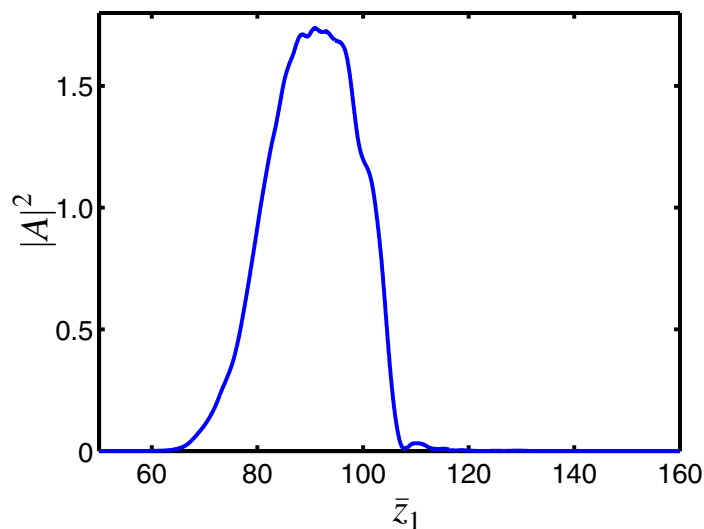


Figure 21. The scaled power of the output pulse from the low feedback RAFEL simulation with feedback fraction $F = 1 \times 10^{-5}$. The pulse shown has a time–bandwidth product of $\Delta\nu\Delta t \approx 1.3$.

and a shorter rms pulse length of $\langle\sigma_{z_1}\rangle \approx 8.1$. The mean time–bandwidth product (for the 80 post-saturation passes) is reduced from the SASE result by a factor ≈ 4.6 to $\langle\Delta\nu\Delta t\rangle = 1.35$. The mean peak power was not significantly changed at $\langle|A|_{\text{peak}}^2\rangle \approx 1.9$.

The increase in quality of the pulse output is evident from comparison of the SASE result of figure 20 with 21, which plots the scaled output power of a pulse with a time–bandwidth product of $\Delta\nu\Delta t \approx 1.3$, close to the mean value.

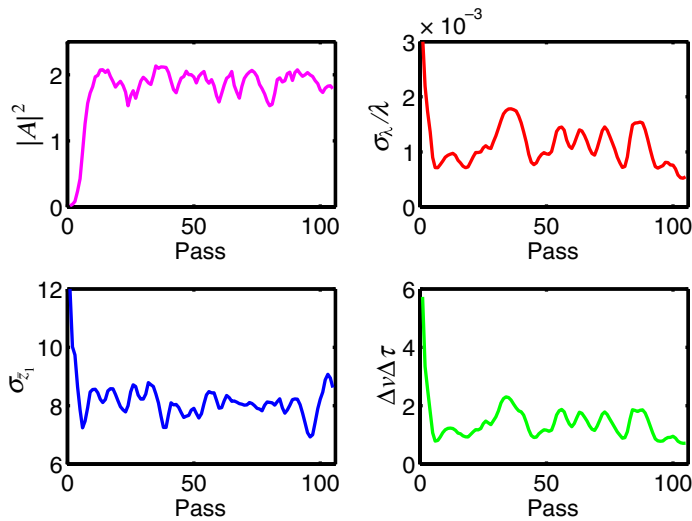


Figure 22. Evolution of low feedback RAFEL radiation pulse parameters as a function of cavity pass number are: the pulse peak intensity $|A|^2$, the rms spectral width σ_λ/λ , the rms pulse length σ_{z_1} and the time–bandwidth product $\Delta\nu\Delta t$. A feedback fraction of $F = 10^{-5}$ was used.

The evolution of the scaled pulse peak power $|A|^2$, the rms spectral width σ_λ/λ , the rms pulse length σ_{z_1} and the time–bandwidth product $\Delta\nu\Delta t$, are plotted from start-up through to deep saturation in figure 22. Despite the low feedback fraction, saturation is seen to occur after around ten cavity passes.

6. Conclusion

The VUV-FEL proposed for the UK 4GLS facility and based on a high-gain amplifier operating with a small feedback, the so-called RAFEL, has been shown via full 3D simulations to provide a relatively robust design which is not particularly sensitive to effects such as degradation of mirror reflectivity. Due to the small amount of feedback, the design allows for the rapid development of temporally coherent radiation pulses that are close to Fourier transform limited. Furthermore, the length of the pulses may be varied via cavity length detuning. The 3D modelling has been made possible by using the FEL simulation code Genesis 1.3 with the optics simulation package, OPC. It was shown that the original parameters of the CDR, developed using only a relatively simple model of the cavity, provided a working design that was close to the optimum.

The 3D capability of the OPC code allows proper modelling of the hole outcoupled cavity and provides important information about the development of the transverse modes. Calculation of both transverse profile within the cavity and in the far-field assist in choice of its geometry and outcoupling hole size. This initial modelling suggests that the VUV-FEL will need two or three outcoupling mirrors with hole radii 1.5–2.5 mm to cover the 3–10 eV operational range of photon energies. However, further work will be required in this area to refine the design.

Engineering studies are ongoing to investigate the effects upon the cavity mirrors of the high average power of the VUV-FEL. The output power ranges from ~ 300 W, for operation

at $4\frac{1}{3}$ MHz, to potentially ~ 90 kW for operation at the maximum ERL SCRF frequency of 1.3 GHz. The power distribution on the DS mirror, as shown in figure 7, has been converted into an input power distribution for finite element simulations of the mirror, assuming a reflectivity of 60%. Although at the minimum repetition rate of $4\frac{1}{3}$ MHz the total absorbed power is only 24 W, and the simulation assumes that the mirror is mounted in a water cooled copper block, the absorbed power is sufficient to cause a temperature rise of up to 80 K and a significant change in mirror RoC, the effects of which are under investigation through importing the distorted surface of the mirror into the OPC code. It is likely that counter-measures such as a deformable mirror surface or cryogenic cooling will be required and that it will be extremely challenging to increase the repetition rate far beyond $4\frac{1}{3}$ MHz.

A preliminary study in 1D using a very low cavity feedback factor has also shown that a low feedback RAFEL may generate radiation pulses of greatly improved quality than that possible using SASE. When the power feedback is significantly greater than the equivalent shot-noise power, temporal coherence was shown to develop rapidly as a function of cavity round-trip number giving a time–bandwidth product of ~ 1.3 for a cavity power feedback fraction of $F = 10^{-5}$. This was nearly a factor of five better than that of the equivalent SASE result. The method of attaining the low feedback factors were not discussed, however the fact that they may be so small indicates that there is significant scope in extending the low feedback RAFEL concept into the XUV and possibly further. The possibility of combining harmonic generation methods [26]–[29] and RAFEL also exists and these exciting possibilities will be the subject of future research.

Acknowledgments

We are grateful for helpful discussions with Elaine Seddon, Wendy Flavell, Mike Poole and Jim Clarke. We would also like to acknowledge the support of the Science and Technology Facilities Council and the Scottish Universities Physics Alliance and the valuable contributions of the 4GLS International Advisory Committee. This work has been supported in part by the EU Commission in the Sixth Framework Program, contract no. 011935-EUROFEL.

References

- [1] Poole M W and Seddon E A 2005 *Proc. 2005 Particle Accelerator Conf. (Knoxville, Tennessee)* pp 431–3
Joint Accelerator Conferences online at <http://www.jacow.org>
- [2] CCLRC 2001 The Science Case for 4GLS Council for the Central Laboratory of the Research Councils (UK)
online at <http://www.4gls.ac.uk/Documents/EPSRC-Dec2001/Science Case.pdf>
- [3] Flavell W R *et al* 2005 *Proc. SPIE* **5917** 59170C1–8
- [4] Flavell W R, Seddon E A, Weightman P, Chesters M A, Quinn F M, Clarke D T, Clarke J A and Tobin M J
2004 *J. Phys.: Condens. Matter* **16** S2405–12
- [5] McNeil B W J, Clarke J A, Dunning D J, Hirst G J, Owen H L, Thompson N R, Sheehy B and Williams P H
2007 *New J. Phys.* **9** 82
- [6] CCLRC 2006 *4GLS Conceptual Design Report* Council for the Central Laboratory of the Research Councils
(UK) online at <http://www.4gls.ac.uk/documents.htm#CDR>
- [7] McNeil B W J 1990 *IEEE J. Quantum Electron.* **26** 1124
- [8] Faatz B, Feldhaus J, Krzywinski J, Saldin E L, Schneidmiller E A and Yurkov M V 1999 *Nucl. Instrum. Methods Phys. Res. A* **429** 424–8

- [9] Nguyen D C, Sheffield R L, Fortgang C M, Goldstein J C, Kinross-Wright J M and Ebrahim N A 1999 *Nucl. Instrum. Methods Phys. Res. A* **429** 125–30
- [10] Huang Z and Ruth R D 2006 *Phys. Rev. Lett.* **96** 144801
- [11] Thompson N R, Poole M W and McNeil B W J 2005 *Proc. 27th Int. Free Electron Laser Conf. (Stanford, USA)* pp 79–82 Joint Accelerator Conferences online at <http://www.jacow.org>
- [12] McNeil B W J, Robb G R M, Dunning D and Thompson N R 2006 *Proc. 28th Int. Free Electron Laser Conf. (Berlin, Germany)* pp 59–62 Joint Accelerator Conferences online at <http://www.jacow.org>
- [13] Reiche S 1999 *Nucl. Instrum. Methods Phys. Res. A* **429** 243–8
- [14] Karssenberg J G, van der Slot P J M, Volokhine I V, Verschuur J W J and Boller K-J 2006 *J. Appl. Phys.* **100** 093106
- [15] Bonifacio R, Pellegrini C and Narducci L 1984 *Opt. Commun.* **50** 373–8
- [16] Al-Abawi H, Hoff F A, Moore G T and Scully M O 1979 *Opt. Commun.* **30** 235–8
- [17] Colson W B 1990 *Laser Handbook* vol 6 ed W B Colson, C Pellegrini and A Renieri (Amsterdam: North-Holland) pp 117–94
- [18] Piovella N, Chaix P, Shvets G and Jaroszynski D 1995 *Phys. Rev. E* **52** 5470–86
- [19] Jaroszynski D A, Chaix P, Piovella N, Oepts D, Knippels G M H, van der Meer A F G and Weits H H 1997 *Phys. Rev. Lett.* **78** 1699–702
- [20] Nishimori N, Hajima R, Nagai R and Minehara E J 2001 *Phys. Rev. Lett.* **86** 5707–10
- [21] Xie M 1996 *Proc. 1995 Particle Accelerator Conf. (Dallas, USA)* pp 1835 Joint Accelerator Conferences online at <http://www.jacow.org>
- [22] Bridou F, Cuniot-Ponsard M, Desvignes J-M, Maksimovic I and Lemaire P 2004 *Proc. SPIE* **5250** 627
- [23] Volokhine IV 2003 Design and numerical analysis of TUE-FEL II *PhD Thesis* University of Twente, The Netherlands
- [24] Sziklas E A and Siegman A E 1975 *Appl. Opt.* **14** 1874
- [25] Kim K J 1986 *Phys. Rev. Lett.* **57** 1871–4
- [26] Bonifacio R, De Salvo Souza L, Pierini P and Scharlemann E T 1990 *Nucl. Instrum. Methods Phys. Res. A* **296** 787
- [27] Yu L-H *et al* 2000 *Science* **289** 932
- [28] McNeil B W J, Robb G R M, Poole M W and Thompson N R 2006 *Phys. Rev. Lett.* **96** 084801
- [29] McNeil B W J, Robb G R M and Poole M W 2004 *Phys. Rev. E* **70** 035501(R)